A Crustal Velocity Model for Locating Earthquakes in Monterey Bay, California

Article *in* Bulletin of the Seismological Society of America · December 2000

DOI: 10.1785/0120000016

4 authors, including:

Michael Lee Begnaud
Los Alamos National Laboratory
66 PUBLICATIONS **280** CITATIONS
SEE PROFILE

D. S. Stakes
Cuesta College
107 PUBLICATIONS **2,589** CITATIONS
SEE PROFILE

Bulletin of the Seismological Society of America, 90, 6, pp. 1391–1408, December 2000

A Crustal Velocity Model for Locating Earthquakes in Monterey Bay, California

by M. L. Begnaud,* K. C. McNally, D. S. Stakes, and V. A. Gallardo

Abstract The seismicity of the Monterey Bay displays a sparse distribution of events with a majority in northern Monterey Bay, on the San Gregorio fault. The paucity of near-shore and offshore seismic recording instruments and the use of velocity models from inland regions for earthquake hypocentral locations and focal mechanisms have led to uncertainties and inaccuracies for seismic events on major faults that crosscut the Bay. New three-component seismic data were acquired during 1997–1999 by the Monterey Bay Aquarium Research Institute (MBARI) Margin Seismology project using ocean-bottom digital corehole and standard seismometers, and coastal digital RefTek instruments obtained from IRIS-PASSCAL by the University of California, Santa Cruz. We have analyzed phases from earthquakes in the Monterey Bay vicinity located by these instruments and used them to supplement the adjacent coastal stations of the permanent Northern California Seismic Network. A new one-dimensional velocity model for the region requires slow velocities from 2 to 6 km that we attribute to sheared granites observed in the Salinian Block in the center of Monterey Bay. Velocities in the 10–16 km layer are consistent with continental crustal velocities. A sharp increase in velocity at ~16 km suggests a boundary that results from underplating of oceanic crust. This underplated zone appears to extend to a depth of ~27–30 km where we observe normal upper mantle velocities near 8.0 km/sec. New details from the ocean-bottom corehole and coastal RefTek instruments for events along the SGF and Monterey Bay fault zones hint at local fine-scale structures and have implications for tectonic history and plate reconstruction interpretation.

Introduction

The central California continental margin is crosscut by major faults with both onshore and offshore segments characterized by moderate to low seismicity levels (Fig. 1). These faults are part of the modern San Andreas system or inherited structures related to the pre-San Andreas subduction environment or the late Oligocene to early Miocene transition from subduction to transform plate margin (Nicholson *et al.,* 1994; Dickinson, 1997). Like many seismically active sections of the continental margin, there is a historic lack of a sufficient number of near-shore or offshore seismic recording instruments in the vicinity of Monterey Bay (MB) to constrain offshore seismic events. In addition, the use of velocity models from inland regions for earthquake hypocentral locations and focal mechanisms have led to uncertainties and inaccuracies for seismic events within MB.

Accurate hypocenter locations for central California offshore seismic events are important for a variety of reasons. First, the San Gregorio fault is the second-most hazardous fault in the MB coastal region, following the San Andreas. It is a Class A fault, with a significant magnitude potential ($>M6$) and a geologic slip rate ranging from at least 5 mm/yr up to 10 mm/yr (Weber, 1990; Kelson *et al.,* 1992; Working Group on Northern California Earthquake Potential, 1996; Simpson *et al.,* 1997; Peterson *et al.,* 1998). Second, the San Gregorio fault (SGF) and the Monterey Bay fault zone (MBFZ) are adjacent to the highly populated Santa Cruz and Monterey Peninsulas. Clearly, it is very important to evaluate the fault hazards and earthquake fault mechanics of the local coastal margin as well as the crustal velocity structure and active tectonics. Lastly, the offset history of the major transform systems is a key to consistent models for the mid-Tertiary plate reorganization and the formation and northward migration of the triple point. The origin, dismemberment, and accretion of the Salinian terrane are constrained by the major faults of this system. The distribution of modern seismicity, discernment of older structures, and

*Present address: Los Alamos National Laboratory, EES-3, MS D408, Los Alamos, New Mexico, 87545.

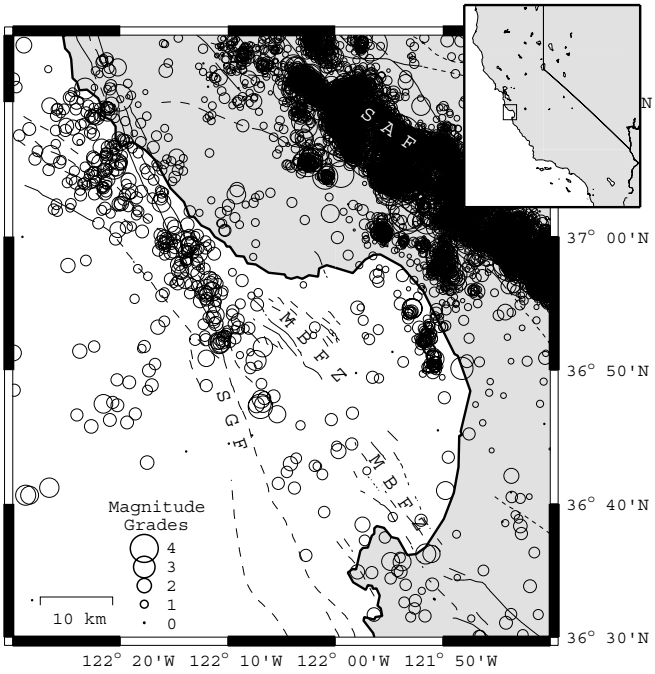

Figure 1. Seismicity for the Monterey Bay coastal region from 1984 to March 1999 as cataloged by the NCEDC (Romanowicz *et al.,* 1994). The levels of seismicity for the San Gregorio fault (SGF) and Monterey Bay fault zone (MBFZ) are much lower than for the San Andreas fault (SAF), with the majority of SGF seismicity occurring on the SGF in northern Monterey Bay.

the regional crustal structure may elucidate clues of past fault configurations.

Using public data from the Northern California Earthquake Data Center (NCEDC) (Romanowicz *et al.,* 1994) and new data from seafloor and near-shore seismograph stations, we have developed a new one-dimensional (1D) crustal velocity model for the MB coastal region. This improved velocity model is consistent with regional geology as well as California margin tectonic models (e.g., Page and Brocher, 1993; Nicholson *et al.,* 1994; Holbrook *et al.,* 1996; Dickinson, 1997), and provides more accurate hypocenter locations for seismic events on the offshore segments of the San Gregorio and Monterey Bay fault zones.

Geologic Setting

Monterey Bay, California is a dramatic arcuate incision into the Salinian Block, with submarine exposures of the Cretaceous granodiorite basement overlain by Miocene–Pliocene sediments. The bay is crosscut by active faults of the diffuse MBFZ and bounded on the west by the SGF, which parallels the coastline from Point Sur to Half Moon Bay. The MBFZ is responsible for the internal slivering of the Salinian block (Greene, 1990), defines the major bends of the Monterey Canyon, and may have been a major structure during the mid-Tertiary change in plate motion (Stakes *et al.,* 1999b). The Monterey Canyon (Fig. 2), just north of Monterey Peninsula, follows and has exposed the contact between the highly sheared basement granodiorite and the overlying sediments. The southern canyon escarpment, oriented oblique to the MBFZ, includes vertical shear zones every few tens of meters. Recovered samples from this area include granodiorite with slickensides as well as thick deposits of gouge derived solely from granitic material (Stakes *et al.,* 1999b; D. Stakes *et al.,* unpublished data, 2000).

The SGF, considered the westernmost segment of the San Andreas fault system, forms a relatively straight lineament from Point Reyes to Point Sur, a distance of ~190 km. Movement along this fault system is thought to have initiated only ~11 mybp (Clark *et al.,* 1984), with total offsets estimated between 100 and 150 km (Graham and Dickinson, 1978; Clark *et al.,* 1984). The SGF has subareal exposures at Pescadero Point, ~47 km northwest of Santa Cruz, and Point Reyes (~150 km northwest of Santa Cruz), between San Francisco and Cape Mendocino. The Pescadero Point exposures include late Oligocene to early Miocene basaltic andesites intruded into marine sediments overlying Cretaceous to Paleocene conglomerates of the Pigeon Point Formation. These andesites are similar in age and chemistry to basaltic andesites recovered within MB as well as adjacent subareal exposures (Dickinson, 1997; Stakes *et al.,* 1999b). Cretaceous granodiorites and conglomerates at Point Reyes have similarly been correlated with the Salinian granites and the Carmelo Formation in the MB area (Kistler and Champion, 1997; Clark *et al.,* 1999 and references therein; Stakes *et al.,* 1999b; D. Stakes *et al.,* unpublished data, 2000).

Instrument Deployments

A suite of seafloor instruments was deployed in MB for periods during 1997 and 1998 (Figs. 2–3). As part of the Monterey Bay Ocean-Bottom International Seismic Experiment (MOISE) (Romanowicz *et al.,* 1998; Stakes *et al.,* 1998b), a broadband seismometer and conventional ocean floor seismometers and hydrophones were deployed for three months in 1997. Two Monterey Bay Aquarium Research Institute (MBARI) well-coupled ocean-bottom seismometer packages installed by remotely operated vehicle (ROV) (Stakes *et al.,* 1998a) were included in this deployment. Since the primary goal of MOISE was to demonstrate the usefulness of the broadband instrument package deployed on the seafloor of the continental shelf, the 1997 instruments were positioned for data comparison rather than optimizing azimuthal coverage of the faults. Most of the instruments were placed at the MOISE site on the center of the sedimented Smooth Ridge (40 km west of Moss Landing and west of the SGF), with additional deployments within the MBFZ (Fig. 2).

The MBARI seismometers are short-period instruments designed to be deployed either within a borehole drilled in basement exposures or within a portable pseudo-borehole in

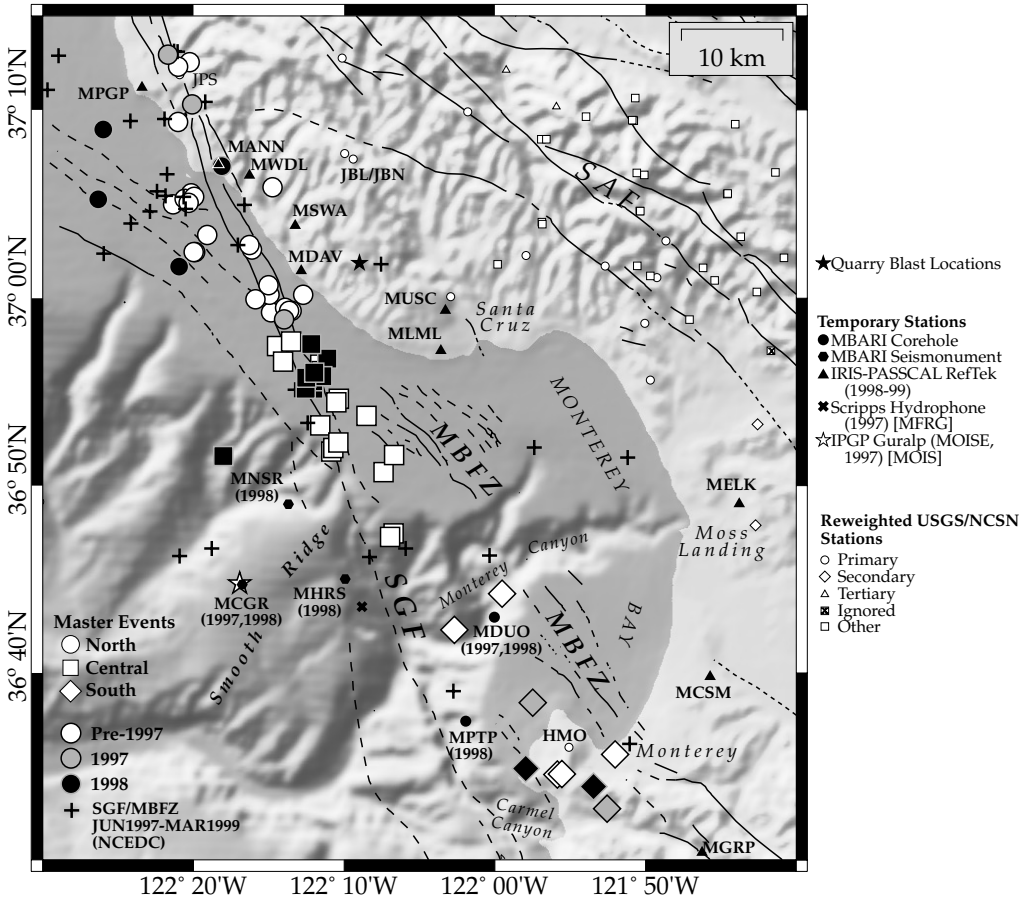

Figure 2. Master events, recent seismicity, and stations used for the one-dimensional velocity inversion. The initial data set involved selecting a series of best-located events (Master Events) from the San Gregorio/Monterey Bay fault zones using the NCEDC locations, categorized into north, central, and southern sections of Monterey Bay. The phases for all NCSN stations were reweighted based on station proximity to the bay, consistency of recording, and relative station location to the San Andreas fault. Only primary (including ocean-bottom and coastal RefTek instruments), secondary, and tertiary stations were used for initial velocity inversion (Table 4).

a cement block, placed on sediment (Stakes *et al.,* 1998a). These corehole seismometers are deployed by a submersible that can unambiguously level and orient the seismic sensors prior to data acquisition. The superior mechanical coupling of these instruments, combined with knowledge of their orientation, permits the acquisition of high-fidelity, low-noise data on both vertical and horizontal channels. This provides more accurate arrival time picks for seismic velocity modeling and, along with the improved azimuthal coverage gained by the use of offshore seismographs, much greater control over hypocenter locations and focal mechanisms (see Begnaud and Stakes, 2000 for a detailed description of how the offshore instruments affect hypocenter and focal mechanism determination).

During 1998, three-component ocean-bottom and traditional land seismometers were deployed in and around Monterey Bay to maximize azimuthal coverage of earthquakes on the SGF in the northern and central parts of MB, where earthquake activity is greatest. MBARI ocean-bottom instruments were deployed for approximately nine months, with three or more instruments operating for over 240 days (Fig. 3). Basement borehole sites include MDUO and MPTP (Fig. 2) and are within the MBFZ, east of the San Gregorio at a depth of about 1000 m. MBARI deployment sites to the west of the SGF, at different locations on the sedimented Smooth Ridge, required the use of cement blocks for instrument installation.

In addition to the seafloor instruments, RefTeks (provided by IRIS-PASSCAL) were deployed from 1998 to July 1999 at 10 nearshore sites around MB. These coastal instruments were deployed in order to increase the number of land instruments between the San Andreas fault and the SGF and improve coverage of Monterey area earthquakes. Information for both the ocean-bottom and coastal temporary stations is listed in Table 1.

From June 1997–March 1999, there were 63 NCEDC

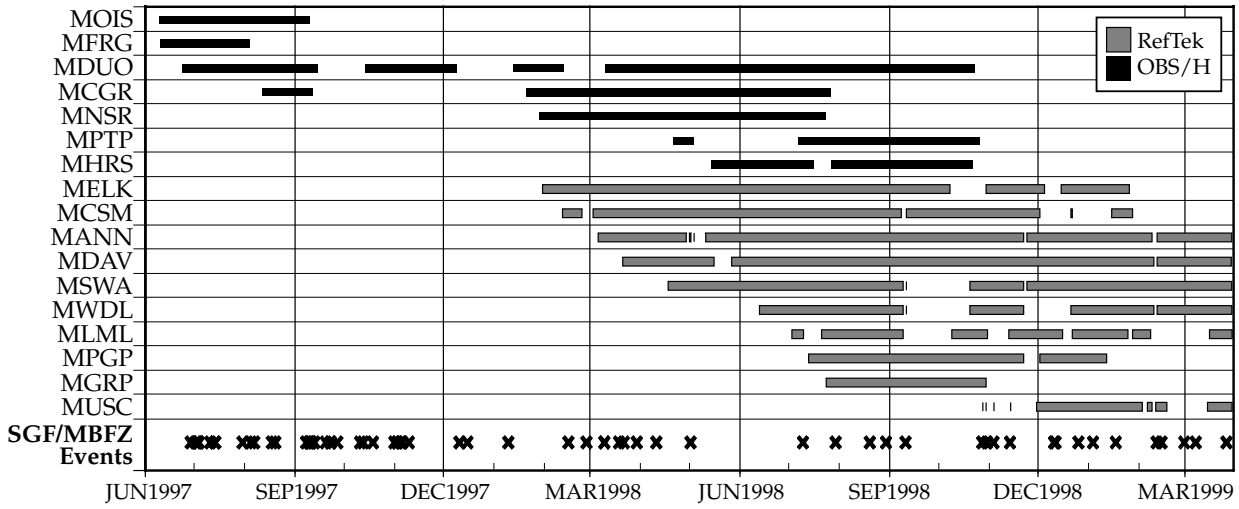

Figure 3. Dates of operation for the MBARI ocean-bottom and RefTek coastal instruments from June 1997 to March 1999. Also shown are times of San Gregorio fault (SGF)/Monterey Bay fault zone (MBFZ) events (Fig. 2).

Table 1
Ocean-Bottom and Coastal Station Information

Station	Lat (°N)	Lon (°W)	Elev. (km)	Number of SGF/MBFZ Events Detected Jun–Dec 1997	1998	Jan–Mar 1999	Magnitude Range
			Ocean-Bottom				
MCGR	36.7456	122.2795	−1.003	6	8		1.1–2.4
MDUO	36.7164	122.0008	−0.968	19	10		0.9–3.8
MFRG	36.7258	122.1470	−1.250	3			0.9–3.8
MHRS	36.7503	122.1653	−0.821		5		1.4–1.9
MNSR	36.8168	122.2282	−0.778		8		1.1–2.4
MOIS	36.7461	122.2823	−1.016	10			0.9–3.8
MPTP	36.6239	122.0325	−0.621		5		1.4–1.9
			Coastal				
MANN	37.1186	122.3061	0.004		15	4	1.0–2.7
MCSM	36.6632	121.7623	0.090		8	1	1.4–2.7
MDAV	37.0239	122.2146	0.009		14	5	1.0–2.7
MELK	36.8171	121.7301	0.054		9	1	1.4–2.7
MGRP	36.5066	121.7707	0.090		5		1.4–1.9
MLML	36.9533	122.0600	0.010		7	2	1.4–2.7
MPGP	37.1863	122.3903	0.010		6	0	1.5–2.7
MSWA	37.0642	122.2212	0.011		11	6	1.0–2.7
MUSC	36.9889	122.0549	0.090		7	4	1.0–2.7
MWDL	37.1085	122.2715	0.010		10	4	1.1–2.7
	SGF/MBFZ Events Listed by NCEDC:			25	21	6	
	Magnitude Range:			0.5–3.8	1.0–2.7	1.0–1.7	0.5–3.8

cataloged events on the SGF and/or MBFZ, within and adjacent to MB (area defined in Figure 2), available for use in the determination of the improved crustal velocity model, 46 of which occurred during ocean-bottom and/or the coastal RefTek deployments. The phases from the ocean-bottom and coastal instruments were used to supplement data acquired through the NCEDC for MB events from the past 15 years (Fig. 1). The use of ocean-bottom and coastal data provided key ray paths along and across the SGF and MBFZ for the velocity inversion.

One-Dimensional Velocity Inversion

Figure 4 displays the regions defined for specific velocity models used by the U. S. Geological Survey (USGS)-Northern California Seismic Network (NCSN) for locating earthquakes in the Monterey area. Both the Loma Prieta-Pacific (LOM) (Dietz and Ellsworth, 1990) and Central Coast (CST) (Oppenheimer *et al.,* 1993; Dorbath *et al.,* 1996) models are inland and/or distant from Monterey Bay. When determining the event location, if an epicenter falls within a dashed zone, then nearby models and station delays are combined into hybrid models/delay sets to locate the earthquake. The majority of Monterey earthquakes are located in northern MB, along the SGF, where the outer dashed regions for the CST and LOM models intersect; the bulk of these events would be located using a hybrid model/delay set. Unfortunately, the use of these hybrid models and delays do not produce consistent location results. A velocity model and station delay set specific for events in MB can improve event locations significantly.

Master Event Determination

The best-located earthquakes along the San Gregorio fault were used as a starting point for calculation of a new velocity model. To determine the best-located events within MB, we analyzed phases for NCSN coastal stations near the SGF. Since the majority of the earthquakes in MB are located on the SGF, arrivals were analyzed at specific NCSN stations approximately located in-line with the SGF trace. Four NCSN stations were chosen as select stations, two north (JPS, JBG) and two south (HMO, BPR) of MB (JPS and HMO, see Fig.

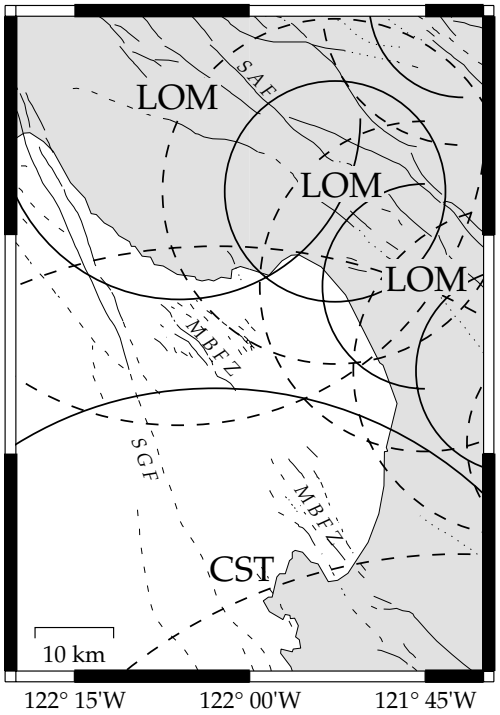

Figure 4. Regions defined for specific velocity models used by the USGS/NCSN for locating earthquakes in the Monterey area (adapted from Oppenheimer *et al.,* 1993). Solid lines indicate where a specific velocity model is used, and dashed areas indicate where hybrid models are used. If an epicenter falls within a hybrid zone, then nearby models and station delays are combined to locate the earthquake. The majority of Monterey earthquakes are located along the San Gregorio fault in northern Monterey Bay where the outer dashed regions for the USGS models CST and LOM intersect. The use of hybrid models and delays for locating these events do not produce consistent locations and depths.

2). The criteria for selecting these master events began with checking errors in location using USGS velocity models and the HYPOINVERSE location program (Klein, 1989). Phase data were checked for all events along the SGF from 1984–1998 to determine if they were detected from at least one of the select stations both north and south of the bay.

Events that passed the above test parameters were further classified into subregions based on similar locations: north (latitude $>$ 36°58′N), central (36°58′N $\leq$ latitude $>$ 36°45′N), and south (latitude $\leq$ 36°45′N) (Fig. 2). Common features for events in these regions were examined, and then each event was evaluated for stability in apparent velocities. Any event displaying anomalous apparent velocities or location errors was removed from the data set, leaving 65 master events (Table 2).

Starting Velocity Model and Delays

The starting one-dimensional velocity model (San Gregorio, SGO) was developed using phases from the select stations above to provide information on layer velocities within the bay. We constructed a homogeneously layered velocity model based on travel-time plots and comparisons with existing velocity models for the area (Fig. 5) (Table 3). Using a gradient version of this new velocity model (using TTGEN [Klein, 1989]), we first relocated the master events in the bay (HYPOINVERSE location program, no station delays) and determined that the SGO model was stable. The SGO model displays significantly slower velocities (by ~0.5–1.25 km/sec) in the upper 10 km than any of the three frequently used USGS models for the area (LOM, CST, and San Francisco peninsula [PEN] [Olson, 1986]) (Fig. 5). Travel-time residuals were surprisingly low when comparing NCSN stations using different USGS models to those residuals using SGO, which reconfirmed that the SGO model was locating events more accurately.

Station delays and *S* phases were then evaluated using the SGO model. Comparing t_s versus t_p suggests a higher V_p/V_s ratio for the bay (1.77) that is best explained by slower shear velocities. The updated ratio was then included in locating the events. The USGS routinely uses *S*-wave station delays based on a V_p/V_s ratio applied to the *P*-wave station delays for locating events. Analyzing *S*-wave residuals for the NCSN stations suggests this is not always valid. For the SGO model, we used a velocity model for *S* waves based on our updated V_p/V_s ratio and the corresponding *P*-wave station delays. Only one NCSN station (JBL/JBN) (Fig. 2) consistently reported enough *S*-wave arrivals to justify calculating an independent *S*-wave delay. Using the *S* waves in this manner, we obtained better hypocentral depths and a corresponding reduction in the calculated vertical error. All coastal and ocean-bottom stations are three component (except MFRG, Fig. 2) and provide critical *S*-wave arrivals to constrain focal depths. These new hypocentral locations form the starting data set for a 1D velocity inversion discussed below.

Phase Data

Before velocity inversion was performed, the phase data were analyzed to remove travel-time outliers. All stations were reweighted, strengthening the use of the ocean-bottom and coastal data and providing a travel-time data base centered more on the bay rather than further inland.

The analysis of the phase data began by using the SGO model on original NCEDC and MBARI/RefTek phase data to obtain phase information relative to the model. The phases were reweighted based on a primary, secondary, tertiary, and ignored station list (Table 4). The first three comprise the master station list and were compiled with the NCSN stations based on station proximity to the bay and a consistency in recording history (Fig. 2) (53 stations, 36 NCSN, and 17 MBARI/RefTek). Phases with source-station distance greater than 100 km were weighted so as to remove them from consideration concerning event location and origin time. This step displayed the effect of shallow structure on event location. To determine how distant phases ($>$100 km) were

Table 2
Master Events for Preliminary Velocity Inversion

Date/Time (UT)	Lat (°)	Lon (°)	Depth (km)	Mag
09/25/1984 02:29:56	36.5765	−121.9303	2.55	2.5
09/25/1984 02:47:06	36.5768	−121.9258	2.43	2.5
01/05/1985 07:27:14	36.9110	−122.1725	5.71	2.1
01/09/1985 02:39:07	36.9077	−122.1750	5.46	2.4
04/16/1985 20:04:46	36.7912	−122.1120	6.30	2.3
09/15/1985 20:27:24	36.9335	−122.1980	6.15	1.9
05/07/1986 19:57:52	37.0987	−122.2458	16.93	2.2
10/22/1986 03:50:03	37.2095	−122.3370	14.71	2.4
05/12/1987 02:29:14	37.0435	−122.2682	14.51	2.6
05/16/1987 15:34:57	37.0475	−122.2712	13.79	1.9
08/13/1987 15:14:04	36.5942	−121.8667	4.94	2.8
09/28/1987 08:48:58	36.9413	−122.1927	5.96	1.9
06/22/1989 18:35:33	36.8457	−122.1228	2.11	2.8
06/24/1989 17:05:19	36.8612	−122.1110	0.08	2.7
10/20/1989 03:43:13	36.9878	−122.2472	8.53	2.0
10/31/1989 04:53:45	36.9580	−122.2407	5.78	2.4
11/07/1989 23:22:13	36.9618	−122.2252	9.66	2.9
12/22/1989 01:11:06	36.9897	−122.2280	6.83	2.2
02/11/1990 19:19:48	36.8640	−122.1805	6.17	2.3
03/27/1990 17:04:20	37.0835	−122.3555	9.56	2.0
04/09/1990 09:39:54	37.0032	−122.2488	9.40	2.0
08/29/1990 10:31:36	37.0413	−122.3313	10.99	2.0
09/01/1990 07:58:17	37.0413	−122.3327	11.44	2.0
02/21/1991 12:48:42	37.0932	−122.3358	11.43	2.3
04/23/1991 08:12:32	37.0562	−122.3178	11.36	2.2
06/28/1991 09:26:50	37.0883	−122.3428	15.49	3.6
07/24/1991 00:26:02	36.8673	−122.1782	5.30	2.8
08/09/1991 17:07:04	36.9918	−122.2315	12.47	3.4
01/26/1992 05:29:40	36.8872	−122.1927	5.80	2.0
06/04/1992 14:38:08	36.7378	−121.9918	13.91	2.1
12/28/1992 05:46:19	36.8957	−122.1420	11.45	1.8
04/13/1993 09:05:41	37.0118	−122.2500	7.65	1.9
06/16/1993 15:54:08	37.1563	−122.3500	17.15	2.6
08/22/1993 14:25:33	36.9438	−122.2338	3.26	2.2
08/31/1993 22:39:16	36.9357	−122.1915	5.59	2.1
11/14/1993 03:35:45	36.9992	−122.2647	9.63	2.0
06/02/1994 20:51:09	36.9893	−122.2245	6.50	2.5
06/16/1994 15:10:07	37.2053	−122.3502	17.19	1.9
06/22/1994 07:06:11	37.0032	−122.2118	5.42	1.6
01/12/1995 23:42:39	36.7883	−122.1158	3.55	3.5
06/02/1995 12:00:21	36.8720	−122.1727	5.89	2.0
03/19/1996 09:50:14	36.9893	−122.2270	6.65	2.1
03/02/1997 02:37:47	36.7055	−122.0445	8.27	1.6
05/24/1997 19:18:43	37.0902	−122.3322	4.12	1.7
05/25/1997 00:39:35	37.0848	−122.3385	4.86	2.0
07/04/1997 14:33:37	36.9815	−122.2325	6.21	1.9
07/14/1997 06:11:12	37.1720	−122.3347	13.97	3.8
08/07/1997 00:04:25	36.6405	−121.9578	12.95	2.1
09/11/1997 11:10:00	37.2162	−122.3610	15.76	1.7
12/11/1997 13:54:05	36.5458	−121.8755	8.47	1.6
01/10/1998 01:29:11	37.0282	−122.3490	3.00	1.2
02/27/1998 18:23:22	36.5817	−121.9658	13.75	2.0
03/10/1998 06:55:31	37.1175	−122.3015	6.49	1.5
03/10/1998 21:22:59	36.9467	−122.1852	9.02	2.4
03/19/1998 16:35:31	36.9197	−122.2007	6.47	1.9
03/22/1998 14:16:02	37.0882	−122.4385	11.18	1.5
07/10/1998 16:10:12	36.9265	−122.2007	8.28	1.9
07/30/1998 13:33:27	36.9597	−122.2027	4.63	1.5
08/30/1998 14:54:52	36.5655	−121.8903	9.37	1.5
09/11/1998 04:28:27	37.1500	−122.4327	6.50	1.5
10/28/1998 08:13:54	36.9197	−122.2092	6.74	1.9
10/31/1998 08:38:11	36.9310	−122.1907	7.48	2.6
11/04/1998 16:02:14	36.9295	−122.2082	4.55	1.7
11/14/1998 21:29:36	36.9343	−122.1997	9.00	2.7
12/11/1998 12:55:09	36.8600	−122.3000	6.28	1.1

Locations from N. California Earthquake Data Center

distributed, we constructed new travel-time curves by azimuth. Coastal station residuals were less than those for stations east of the San Andreas as expected. We thus reweighted phases between 100 and 200 km and used them in the inversion to allow deeper penetrating rays. Again the event locations were tested using reweighted phases and the SGO model. The final step was to remove any phases that had low ($\leq$0.25) actual weights used from the HYPOINVERSE program, which had the effect of removing phases with high residuals. The SGO model was used to locate the master events after this last phase-cleaning process, with only stations on the master station list.

Initial Velocity Inversions

We tested whether the original master events along the San Gregorio required the separation into north, central, and south subregions before velocity inversion by examining travel-time curves using all of the master stations. There was no significant observable difference in travel times for different regions of the SGF in MB; thus, we grouped all San Gregorio events together for the velocity inversion. However, beyond an epicentral distance of ~75 km, the spread in travel times was significant and could create errors in the inversion.

We used VELEST, the 1D velocity inversion program of Kissling *et al.* (1994), which solves for a homogeneously layered velocity model while simultaneously solving for hypocenters and station delays. The NCSN station JPS (Fig. 2) was chosen as the reference station for calculating station delays due to its recording history, location within the study area, initial *P*-delay estimate near zero, and number of *P* phases used for the velocity inversion. Station elevations were included in the velocity inversion to allow more accurate ray tracing.

In order to adjust for the travel-time spread, we limited the use of master event travel times to those within an epicentral distance of 75 km and only included those stations on the master station list. For the SGO model, this allowed the use of 1929 *P* phases and 140 *S* phases. Even though the number of *S* phases was low and the VELEST output shear velocities were ignored, we chose to include them in the inversion, which had the effect of stabilizing the hypocentral depths (Kissling *et al.,* 1994). Using only data within a 75-km distance constrained seismic rays to maximum depths of ~12–15 km; to determine deeper velocity structure, a larger data set was required.

Since we were the most confident in the travel times from the master events, output velocities from the inversion for the upper 15 km were heavily damped, to the point of being fixed, and used as the starting model for another in-

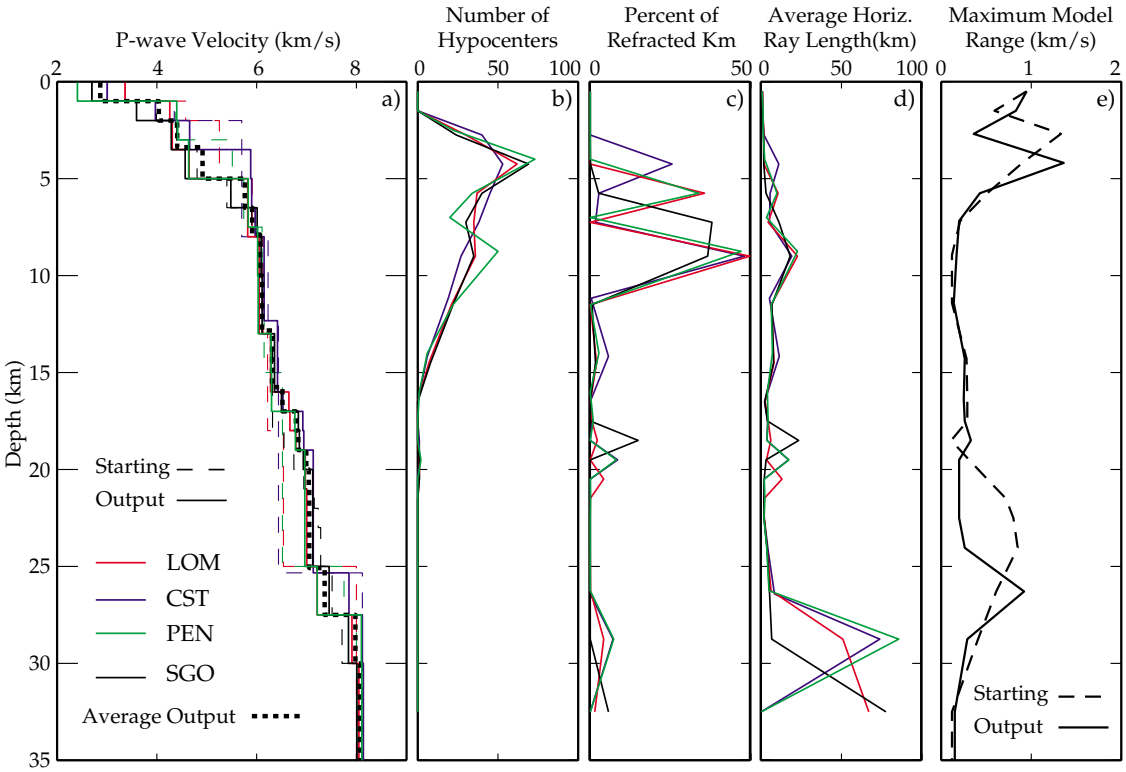

Figure 5. Results of preliminary inversion using different starting models. (a) Output velocity models using the four starting models: Loma Prieta-Pacific (LOM, USGS), Central Coast (CST, USGS), San Francisco Peninsula (PEN, USGS), and SGO (this study) (see text). Different starting models were used to test the dependence on changes in starting model. Models SGO, LOM, and PEN produce similar output models. The CST-derived model displays faster output velocities from ~3.5 to 5 km and from ~25 to 27.5 km. The four graphs to the right (b–e) display inversion characteristics for each starting model. The most highly sampled interval is from ~5 to 12 km where (c) Percent of Refracted Km displays values of up to 50%. The average horizontal ray length (d) is greatest below 25 km where P_n rays are turning. (e) The Model Range graph displays the maximum range of all four starting models before and after the inversion. Ideally, model range should be near zero after the inversion. The model range generally remained higher when the starting range was high. Because of the slight starting model dependence, we chose to use the average of the four output models as a starting model for a final inversion (heavy dotted line).

version with a larger data set. In addition, velocities at the lower boundaries of the starting model (30–35 km) were held fixed at 8.0 km/sec. The larger data set was compiled from MB/SGF earthquakes from 1984–March 1999 (Fig. 1) with phase data outliers removed using the process described previously. Only those events with a minimum of 20 phases, a hypocentral depth greater than 2 km, a horizontal error <3 km, and a vertical error <5 km were allowed for the final data set of 208 events. We chose to use a relatively high maximum vertical error because of the typically wide azimuthal gaps, often observed for events in the bay, that commonly produce larger vertical location errors. Only phases with epicentral distances <200 km were included in the data set that resulted in a total of 6255 *P* and 175 *S* phases. We also included 101 more NCSN stations in the station list (Table 5) for inversion to permit deeper penetrating rays and to better resolve the deeper velocity structure. No NCSN stations east of the San Andreas were included, except a few that were within ~5 km and one within ~10 km.

Along with the SGO model, we also performed the same data removal and inversion steps using the three other USGS velocity models commonly used for locating MB area earthquakes (LOM, CST, and PEN); the results of these inversions are shown in Figure 5. All of the starting models were configured to allow velocity variations similar to those permitted for the SGO model.

Output Velocity Models and Station Delays

Figure 5a shows the output velocities using the existing MB area 1D velocity models as starting models. All starting models produce similar results after the velocity inversion. In particular, three of the starting models (SGO, LOM, PEN) result in output models with slower velocities in the upper ~5 km and faster velocities from depths of ~16–22 km,

Table 3
Velocity Models Specific to Monterey Bay, California

SGO		MON	
Velocity (km/sec)	Depth (km)	Velocity (km/sec)	Depth (km)
2.75	0.0	2.87	0.0
3.50	1.0	3.51	1.0
4.50	2.0	4.06	2.0
4.85	3.5	4.49	3.4
5.30	5.0	5.79	5.0
5.90	6.5	5.80	6.5
6.10	8.0	6.02	7.9
6.20	10.0	6.06	10.0
6.30	13.0	6.10	12.8
6.35	16.0	6.42	15.8
6.45	18.0	6.82	17.0
7.10	20.0	7.00	18.0
7.80	22.0	7.01	19.0
8.00	25.0	7.01	20.0
8.01	30.0	7.03	21.0
8.02	35.0	7.03	22.0
		7.03	23.0
		7.27	25.1
		7.81	27.5
		8.07	30.0
		8.07	35.0

Table 4
Categories for Reweighted NCSN Stations

Primary	Secondary	Tertiary	Ignored
BCG	HAZ	HBT	BAP
BJC	HCB	JBM	BBN
BJO	HCO	JHP	BLR
BPC	HDL	JLX	BPI
BPF	HER	JPP	BSG
BPO	HFP	JSS	BVL
BPR	HJG		HPR
BSR			HSF
BVY			
HMO			
JBC			
JBG			
JBL			
JBN			
JBZ			
JEC			
JEL			
JPL			
JPS			
JRG			
JSM			
JTG			
JUC			

All ocean-bottom and coastal stations in Table 1 are categorized as primary stations

Table 5
Additional NCSN Stations Included for Inversion with Large Data Set

BCW	JLH	NFR	PIV
BEH	JLT	NLN	PKY
BHR	JMB	NOM	PLO
BHS	JMG	NPR	PMC
BMC	JPQ	NRL	PMG
BMH	JQB	NTA	PMM
BRV	JQE	NTB	PMP
BSB	JQN	NTP	PPB
BSC	JQO	PAD	PPC
BSL	JQS	PAN	PPF
BSM	JQW	PAP	PPR
GAF	JRR	PBR	PPT
GGU	JSA	PBW	PRP
GHC	JSC	PBY	PSA
HCC	JSF	PCB	PSC
HCR	JSG	PCG	PSE
HGW	JSGB	PCL	PSH
HNU	JSL	PGH	PSI
HOR	JSP	PHA	PSM
JAL	JST	PHC	PST
JCH	JTR	PHF	PTA
JEG	JWS	PHG	PTF
JEM	NAB	PHO	PTY
JHL	NBO	PHP	PVC
JJR	NFI	PHS	PWK
JKR			

compared to USGS starting models. This suggests that these velocity structural features are not artifacts and are required by the travel-time data. Figure 5b–d displays plots of ray path statistics and density relative to depth and indicate that the shallow and deeper structural anomalies in all the output models are well constrained. There is significant variability in starting models for regions in the shallow (<6 km) and deeper crust (~20–27 km) (Fig. 5a and e). This directly relates to variability in the output velocity models and may indicate zones of high and low ray coverage (Fig. 5e).

Figure 6 shows lateral and vertical ray sampling for the master events. The shallow features observed from the inversion of the master event data constrain velocities mostly for the northern MB area near the coastline, extending to approximately the middle of the bay (Fig. 6a). The addition of the ocean-bottom and coastal temporary stations provide key rays paths within ~25 km of the master events, increasing ray path density by ~28% over using NCSN stations alone (Fig. 6b).

Figure 7 shows lateral and vertical ray sampling for the larger data set only for those rays with midpoints below 12 km depth. The intermediate velocities from ~16 to 22 km depth in Figure 5a are constrained by rays turning in the center of MB and extending somewhat to the northwest. The majority of rays in this figure have midpoints at ~18 km. Rays with midpoint depths of ~30 km sample the upper mantle within and directly north and south of MB.

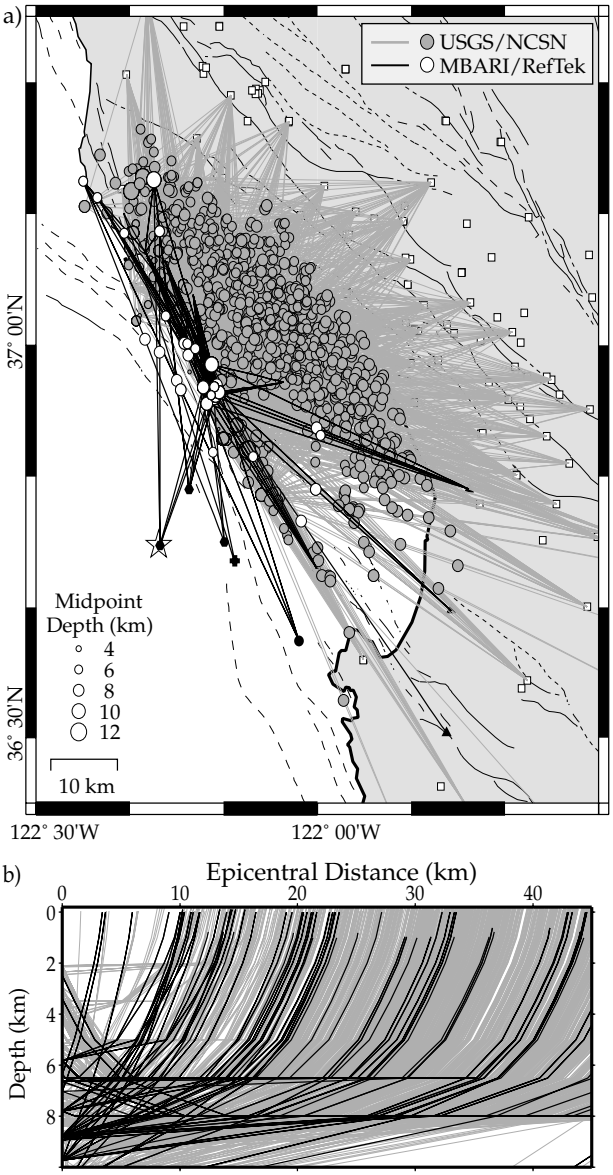

Figure 6. Ray paths and midpoint depths for the master events used in the velocity inversion. Midpoints located directly at epicenter locations indicate direct rays. The rays mostly sample crust between 4 and 8 km along the Monterey Bay fault zone region. (a) Rays and midpoint depths highlighting those for the MBARI ocean-bottom/coastal RefTek instruments, which sample crust mostly along the San Gregorio fault trace; (b) rays paths versus epicentral distance from source. The ocean-bottom and coastal instruments increase ray path density by ~28% within 25 km for source points. This helps to constrain the shallow crustal structure around the San Gregorio and Monterey Bay fault zones.

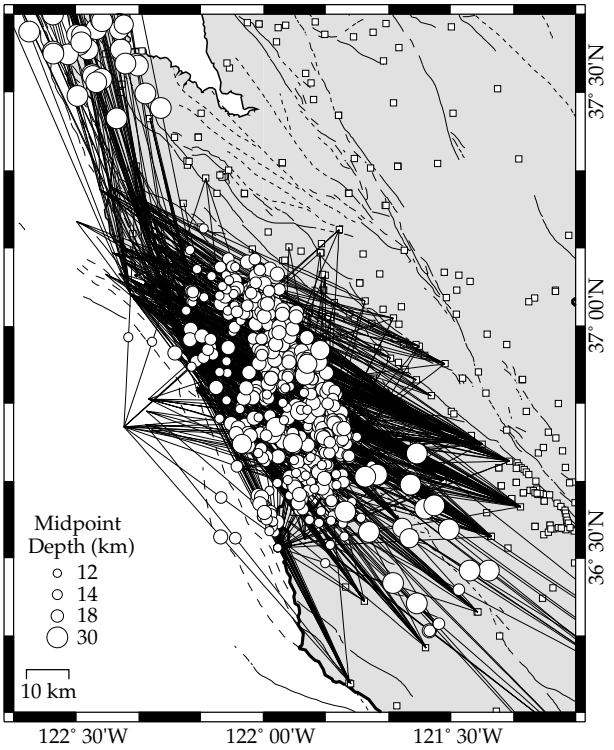

Figure 7. Ray paths and midpoint depths for the select events from the larger 1984–March 1999 San Gregorio/Monterey Bay fault zone data set used for velocity inversion. Midpoints located directly at epicenter locations indicate direct rays. Only those rays with midpoint depths ≥12 km are displayed to reveal lower-crustal sampling. The faster velocities observed between ~15 and 25 km are constrained by rays with midpoint depths within Monterey Bay.

Final Velocity Model

Since the output velocities from the different starting models display slight model dependence, we chose to perform a final velocity inversion, using the average output velocity model from Figure 5a as the starting model and the two-step inversion process described above. This should remove any model dependence for the inversion and provide a more robust solution. Station delays were calculated in a third inversion step (Table 6), holding the velocities fixed and using output locations from the larger data set from the second inversion step. Station elevations were not included with this third step in order to have station delays for use with the HYPOINVERSE location program, which does not consider station elevation for locating events (Klein, 1989).

The final 1D velocity model (denoted MON model) is shown in Figure 8 and listed in Table 3. We have plotted the gradient versions of the USGS models LOM, CST, PEN, and the MON model from this study for comparisons (gradient model of MON determined using TTGEN program). Also shown are a 1D model for the MB area (S. Ross, personal comm., 2000) using data from only NCSN stations and a 1D cut along the SGF section of a two-dimensional forward

Table 6
Station Delays for MON Model

Station	Delay (sec) R*	N*	C*	S*	W*	Station	Delay (sec) R*	N*	C*	S*	W*	Station	Delay (sec) R*	N*	C*	S*	W*	Station	Delay (sec) R*	N*	C*	S*	W*
BAV	0.19	−0.02	0.35	0.44	0.34	CPL	0.07	−0.24	0.07	1.15		HOR	0.17	−0.16	0.23	0.48	0.19	JTR	−0.16	−0.23	−0.28	0.13	
BBG	0.43	0.12	0.59	0.40		CPM	−0.20	−0.37	−0.06			HPC	−0.25	0.34	0.26			JUC	−0.34	−0.59	−0.37	−0.15	
BCG	−0.37	−0.46	−0.42	−0.04		CRA	1.17	0.96				HPH	0.61	0.36	0.44			JUM	−0.19	−0.48	−0.23	0.21	
BCW	−0.03	−0.03	−0.13	0.10	−0.41	CRP	0.36	0.10	0.30			HPL	0.13	−0.01	0.01	0.89		MANN†	0.19	−0.03	0.17		
BEH	0.47	0.20	0.61	0.81		CSC	0.10	−0.24	−0.02	1.42	0.23	HQR	0.12	−0.23	0.34	0.45		MBO	0.07	−0.06			
BEM	0.24	−0.06	0.40	0.50		CSH	0.12	−0.48	0.14	1.14		HSL	0.68	0.40	0.77	1.39		MCGR†	0.61	0.80	0.37	0.20	
BHR	0.37	0.25	0.50	0.65		CSL	−0.08	−0.28	0.09			HSP	−0.06	−0.38	−0.16	0.44	−1.76	MCSM†	−0.02		−0.03	0.30	
BHS	0.02		0.32	0.08		CSP	0.21	0.11	0.20			JAL	−0.40	−0.79	−0.30		−0.44	MCU	0.44	0.18	0.62		
BJC	−0.31	−0.42	−0.36	−0.01	−0.62	CSUI	0.06	−0.06				JBC	0.03	−0.23	0.00	0.29	−0.27	MDAV†	0.03	0.02	−0.01		
BJO	−0.38	−0.51	−0.38	0.01	−0.73	CSV	0.85	0.63	1.17			JBG	0.11	0.11	−0.03	0.18	−0.02	MDUO†	−0.07	−0.27	−0.01	−0.03	
BMS	0.80	0.63	0.86	1.05		CVP	0.10	−0.04	0.24			JBL	−0.29	−0.40	−0.38	−0.26	−0.58	MELK†	−0.10	−0.29	−0.04	0.19	
BPC	0.02	−0.17	0.02	0.20	−0.09	CYB	−0.47	−0.57	−0.45			JBM	−0.15	−0.26	−0.22	0.02	−0.28	MFRG†	0.42	0.26			
BPF	−0.19	−0.29	−0.12	−0.13	−0.70	GAC	0.62	0.52				JBN	−0.29					MGRP†	−0.23	0.00	−0.20	0.04	
BPO	−0.19	−0.29	−0.12	−0.13	−0.70	GAR	0.55	0.42				JBZ	0.12	−0.06	0.03	0.42	−0.07	MHRS†	0.49	0.30	0.65	0.07	
BPP	0.10		0.83	−0.02		GAX	−0.47	−0.48				JCB	−0.13	−0.46	−0.17	0.07	−0.41	MLML†	−0.34	−0.39	−0.33	−0.68	
BPR	−0.20	−0.30	−0.27	0.03	−0.82	GBG	−0.07	−0.13				JCH	−0.30	−0.35	−0.39			MNH	0.15	−0.27	0.41		
BRM	1.10	0.79	1.04	1.81		GCR	−0.46	−0.47				JCP	−0.27	−0.36	−0.30			MNSR†	0.83	0.67	0.90	0.46	
BRV	0.56	0.72	0.74	0.65		GCV	−0.37	−0.41				JEC	0.08	−0.17	0.03	0.38	−0.03	MOY	0.27	0.11			
BSC	−0.26	−0.32	−0.14	−0.07		GDC	0.16	0.08				JEG	−0.30	−0.28	−0.43		−0.67	MPGP†	0.10	0.08	0.06		
BSM	−0.06	−0.34	0.04	0.08	−0.24	GDX	−0.38	−0.38				JEL	0.00	−0.20	−0.01	0.26		MPPT†	0.09	−0.09	0.04	−0.04	
BSR	−0.31	−0.52	−0.33	0.07	−0.72	GGP	−0.03	−0.08				JHL	−0.20	−0.57	−0.17	0.19	−0.36	MRF	0.97	0.74			
BVY	−0.38	−0.61	−0.42	−0.04	−0.55	GHC	−0.07	−0.16				JHP	−0.18	−0.21	−0.29	0.44	−0.43	MST	0.53	0.35			
CAD	−0.20	−0.50	−0.26	0.12	−0.19	GMC	0.28	0.20				JJR	−0.09	−0.19	−0.20	0.25	−0.30	MSWA†	−0.12	−0.23	−0.17		
CAI	−0.07	−0.18	−0.13			GMO	−0.65	−0.63				JLA	−0.21	−0.48	−0.20	0.06	−0.18	MUSC†	−0.40		−0.42		
CAO	0.04	−0.31	0.04	0.70	0.38	GPM	−0.31	−0.41				JLP	0.16	−0.07				MWDL†	−0.10	−0.16	−0.15		
CBR	0.40	0.15	0.27			GRT	0.74	0.64				JLT	−0.16	−0.23	−0.28	0.13		MYL	0.05	−0.05	0.40		
CBS	0.70	0.62	0.67	−0.27		GSG	0.80	0.70				JLX	−0.27	−0.51	−0.32	0.01		NBR	−0.39	−0.41	−0.49		
CBW	0.53	0.31	0.21	1.94		GSS	−0.19	−0.23				JMG	−0.40	−0.43	−0.34			NCF	−0.08	−0.18	0.04		
CCHI	−0.09	−0.25				HAZ	−0.37	−0.78	−0.40	0.01	−0.61	JMP	−0.16	−0.29	−0.21			NFR	−0.02	−0.05	−0.01		
CCO	0.40	0.04	0.43	0.83	0.28	HBT	−0.26	−0.54	−0.30	0.09	−1.02	JNA	−0.17	−0.53	−0.07	0.35		NLN	−0.09	−0.22	−0.28		
CCY	−0.43	−0.61	−0.39	0.43		HCA	−0.03	−0.19	−0.22	0.31	−0.13	JPL	−0.05	−0.30	−0.05	0.25		NMC	−0.33	−0.32	−0.55		
CDO	1.06	1.01	0.76			HCB	−0.02	−0.18	−0.06	0.21	−0.03	JPP	−0.03	−0.13	−0.13	0.19		NMW	−0.08	−0.17	−0.17		
CDU	0.89	0.74	0.87			HCO	−0.16	−0.46	−0.10	0.19	−0.30	JPR	−0.17	−0.35	−0.68	4.69		NSP	−0.11	−0.24	−0.41		

CGP	−0.04	−0.31	0.10	0.61		HCP	1.06			1.36		JPS	0.00	0.00	0.00	0.00		NTB	−0.34	−0.34	−0.39	
CGPI	−0.04	−0.31	0.10			HCR	−0.17	−0.53	−0.20	0.21	0.14	JRG	−0.26	−0.50	−0.32	−0.07		NTY	0.06	−0.13	0.50	
CLC	0.25	−0.08	0.46	1.09	−0.04	HDL	−0.33	−0.60	−0.32	0.05	−0.59	JRR	−0.16	−0.47	−0.18	0.11		PAN	−0.31	−0.02		0.92
CMC	0.25	−0.03	0.54	1.88		HER	0.10	−0.15	0.13	0.39	0.01	JSA	−0.46	−0.48	−0.48			PCC	0.39	−0.16	0.55	0.87
CMH	0.24	−0.12	0.32	0.99	0.38	HFE	−0.07	−0.18	−0.07	0.20	3.80	JSB	−0.50	0.59	0.37			PCL	0.56	−0.11	−0.54	1.46
CMJ	0.04	−0.24	0.13	0.81	−0.22	HFH	0.43	0.16	0.46	0.74	0.17	JSC	−0.13	−0.27	−0.23	0.03		PJL	0.37	0.03	0.60	0.13
CML	0.17	−0.16	0.23	1.66		HFP	−0.41	−0.67	−0.42	−0.06	−0.76	JSF	−0.07	−0.17	−0.14	−0.39		PJR	0.37	0.03	0.60	0.13
CMM	0.32	−0.05	0.39			HGS	−0.05	−0.35	−0.19	0.45	−0.22	JSG	−0.13	−0.29	−0.25	0.20		PLO	0.47	0.84	0.69	0.19
CMO	0.88	0.71	0.87			HGW	−0.27	−0.69	−0.34	0.01	−0.48	JSGB	−0.13					PMM	0.56	−0.11	−0.54	1.46
CMP	0.41	0.13	0.33	1.24		HUG	−0.32	−0.57	−0.30	0.03	−0.72	JSJ	−0.01	−0.31	0.19	0.61		PMP	0.37	−0.48	1.89	0.50
CMR	0.23	0.04	0.48	−0.41		HJS	0.19	−0.11	0.16	0.54	0.68	JSM	0.00	−0.11	−0.15	0.14		PPT	0.43	0.07	0.33	0.80
CMWI	−0.13	−0.31	−0.22			HKR	0.46		0.48	1.06		JSP	−0.35	−0.48	−0.54			PST	0.56	−0.11	−0.54	1.46
CNI	0.04	−0.17	0.07			HLP	−0.41	−0.71	−0.43			JSS	−0.26	−0.57	−0.29	0.13		PTY	0.56	−0.11	−0.54	1.46
COS	0.75	0.41	0.64	1.35		HLT	0.15	−0.17	0.01	0.60	0.79	JST	−0.25	−0.62	−0.24	0.11		PVC	0.56	−0.11	−0.54	1.46
CPI	0.45	0.39		0.53		HMO	−0.10	−0.30	−0.03	0.19	−0.53	JTG	−0.17	−0.41	−0.21	0.10						

*R, regional; N, north; C, central; S, south; W = west.

†Denotes MBARI/RefTek stations, all others are NCSN stations.

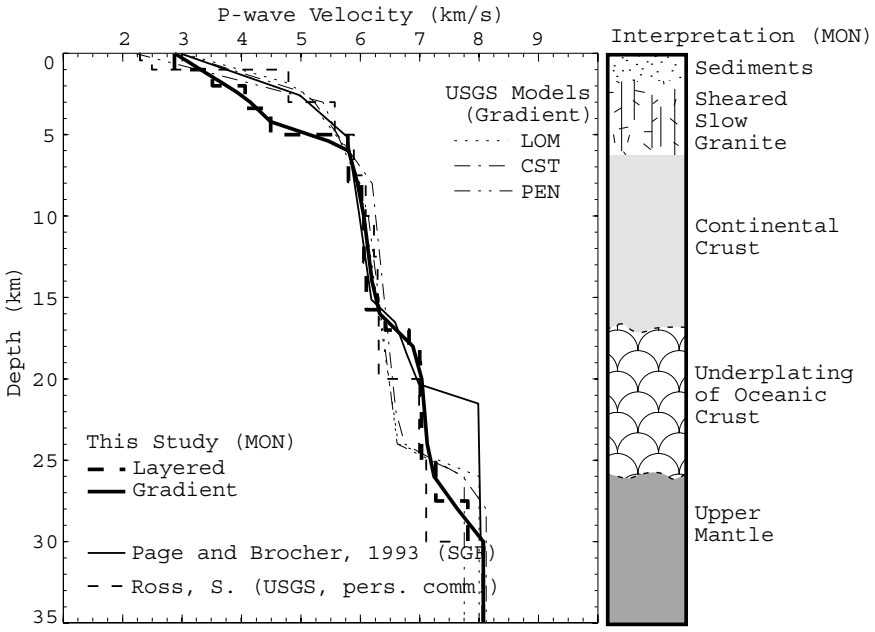

Figure 8. Final velocity inversion and geologic interpretation using average output model from Figure 5 as the starting model. Also shown are the gradient versions of the three area USGS models and the Monterey area models by Page and Brocher (1993) (modified from two-dimensional forward model at San Gregorio fault trace) and S. Ross (personal comm., 2000). The MON models displays two velocity zones that are significantly different than other models. Above ~6 km, the MON model is up to ~1 km/sec slower than the other models. This feature is well constrained as seen from the inversion statistics in Figure 5. From ~6 to 15 km, the MON model is consistent with other models. From ~16 to 25 km, MON is faster than the USGS gradient models, by up to ~0.7 km/sec, and is similar to the Page and Brocher (1993) and the Ross models. MON is slower than the other models from ~25 to 30 km (by up to ~0.5 km/sec, except for the Ross model). We associate the slower shallow velocities in MON to sheared granites in Monterey Bay. Sheared granites have been observed from MBARI remotely operated vehicle observations. We associate the faster/slower velocities from ~16 to 30 km to emplacement of mafic materials at depth by underplating or slab remnants.

model extending from offshore northern MB through the Loma Prieta epicenter (Page and Brocher, 1993).

The MON model displays two significant anomalous velocity zones, when compared with the other velocity models shown in Figure 8. In the upper 2–6 km, the MON model has velocities ranging from 3.5 to 5.8 km/sec, slow relative to other models (~5–5.8 km/sec at similar depths). Velocities from 6 to 15 km are similar to the other models shown (~5.8–6.3 km/sec). From 16 to 20 km, the MON model exhibits velocities similar to the Page and Brocher (1993) model, but has faster velocities (by up to ~0.7 km/sec) compared to the USGS models. At 20 km, the Ross model jumps to values about equal to MON (~7 km/sec) until ~25–28 km where the model becomes slower than MON by ~0.6–0.7 km/sec. At ~21 km, the Page and Brocher (1993) model increases velocity to ~8 km/sec. The USGS gradient models shown become faster than MON below ~25 km until 30 km where they reach a velocity of ~8 km/sec, similar to MON.

Model Reliability

Station Delays and Event Relocations

Calculated station delays for the MON model (Fig. 9a) (Table 6) display a concentration near −0.10 sec with a relatively equal distribution about that point. There are several stations (~13) with delays greater than 0.5 sec. Although the calculated stations delays are not centered about the zero point, we feel they are well distributed given the known lateral heterogeneity in the surface geology for the Monterey Bay area.

We relocated all events from the larger 1984–March 1999 data set using HYPOINVERSE, the MON gradient model and station delays above, and the standard USGS HYPOINVERSE parameters (F. Klein, public ftp site, swave.wr.usgs.gov/pub/outgoing/klein/hypfiles) (Fig. 10). The average root-mean-square (rms) travel-time residual was reduced from 0.12 ± 0.17 sec, for the cataloged locations, to 0.10 ± 0.17 sec, a reduction of 17%. The average horizontal error (ERH) also shows an improvement (1.9 ± 3.2 km), relative to the cataloged locations (2.0 ± 4.4 km), using the MON model. However, the average vertical error (ERZ) does increase from 2.6 ± 5.6 km to 3.7 ± 4.1 km using the MON model, but the standard deviation decreases significantly.

Residual analysis for the larger data set relocations suggests a pattern within the station delays dependent upon epicenter location. To account for this dependency, we chose to recalculate station delays in VELEST separately, using a fixed MON model, for events in the north, central, south, and west part of MB (Fig. 9b–e) (Table 6). These calculated station delays with respect to specific regions of the bay show a transition from more negative delays for northern events to more positive delays for southern events.

Using the MON model and source-dependent delays, we relocated the 1984–March 1999 MB data set (Fig. 10b). The average rms for these relocations is 0.09 ± 0.16 sec, a 25% reduction compared to the catalog locations. The ERH and ERZ values are also similar to those from the relocations using the single regional delay set (1.9 ± 3.8 km and 3.3 ± 3.9 km, respectively), with the ERZ showing slight improvement.

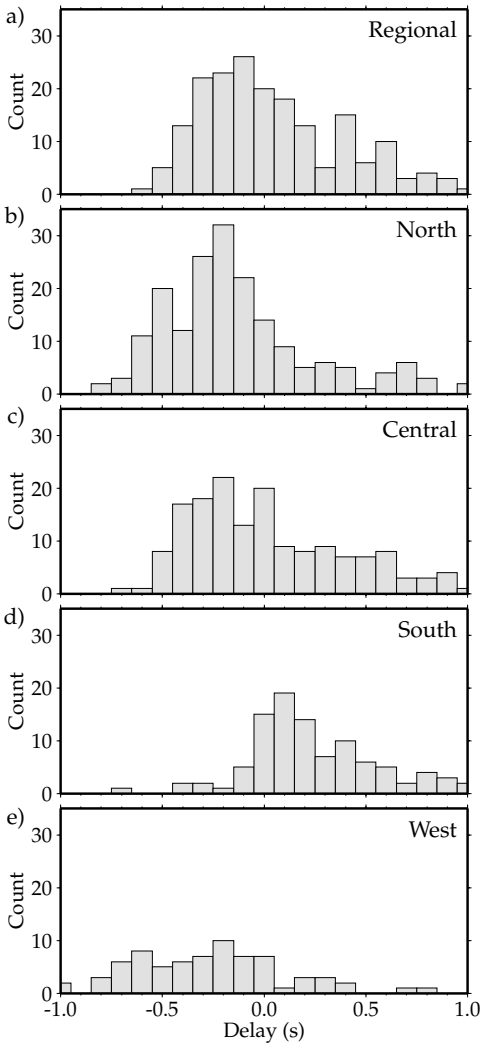

Figure 9. Calculated station delays for the MON model. (a) Station delays for the entire Monterey Bay region. The delays are concentrated near −0.10 sec with a relatively equal distribution about that point. Although the calculated stations delays are not centered about zero, we feel they are well distributed given the known lateral heterogeneity in the surface geology for the Monterey Bay area. (b–e) Source-dependent station delays calculated for regions of the San Gregorio and Monterey Bay fault zones. Differences in source-dependent delays suggest a lateral heterogeneity in the upper crust for the Monterey Bay area.

Using the MON model with source-dependent delays along with the reweighting scheme for the NCSN stations described earlier, we relocated the master events along with earthquakes during the ocean-bottom and coastal instrument deployments (Fig. 11). Since these events were classified as either the "best-located" events or had ocean-bottom/coastal phases, we felt that these events would best demonstrate the seismicity for the SGF/MBFZ in MB. Epicenter locations (Fig. 11a) using the MON model display are more clustered than the catalog locations, with a significant reduction in ERH (0.91 ± 1.12 km to 0.40 ± 0.31 km, 56% reduction). Figure 11b and c display a three-dimensional view of the locations, along the trace of the SGF. Overall scatter is dramatically reduced when using the MON model, with more of an alignment of hypocenters along the trace of the SGF and a hypocenter pattern suggesting an eastward-dipping SGF. ERZ is reduced from 1.32 ± 1.57 km to 1.28 ± 1.86 km. For those events in Figure 11 detected by MBARI ocean-bottom and/or IRIS RefTek instruments, error reduction is greater when using offshore/coastal instruments. ERH is reduced from 1.08 ± 1.73 km to 0.51 ± 0.37 km when including offshore/coastal phases (53% reduction). Similarly, ERZ is reduced by 38% when using phases from offshore/coastal instruments (2.32 ± 3.2 km for NCSN stations only; 1.45 ± 2.33 km for NCSN plus MBARI/RefTek stations).

Comparison of Actual and Calculated Quarry Blast Locations

We tested the reliability of the final MON 1D velocity model by comparing calculated to actual blast locations in a cement quarry northwest of Santa Cruz (Fig. 2). Actual locations were obtained for 13 events in 1997–98, cataloged as blasts by the NCEDC (Fig. 12). The quarry blasts were all located in an area less than 500 m in diameter and provide the only ground truth tests for the MON velocity model.

Using both the single regional delay set and a source-specific delay set, we relocated the 13 quarry blasts using the NCEDC phase data, the MON model (with no offshore/coastal RefTek instrument phases), and a constraint of zero depth (Fig. 12). For comparison, we relocated the events using the USGS location/model parameters (F. Klein, public ftp site, swave.wr.usgs.gov/pub/outgoing/klein/hypfiles), also with a zero-depth constraint (for the quarry area, the LOM model and its station delays are the only model used). The MON model locations using the single regional delay set are an average of 0.65 km closer than the USGS model/delay locations (3.04 km average distance from actual locations). Using the source-dependent delay set (Fig. 12) improved the accuracy even more, to an average of 2.24 km from actual locations. Again, this suggests that the MON model results in more accurate locations whether using a single regional or a source-dependent delay set.

Discussion and Interpretation

Event Relocations and Delays

With the MON model and either the single regional or source-dependent delay set, there is no systematic shift of epicenters in any one direction; rather, there is an overall reduction in scatter for the area, particularly for events along the SGF in northern MB. Locations align more with mapped fault trace orientations compared to events located using USGS models. Depth changes, relative to the original catalog locations (Fig. 10–11), indicate that the MON model reduces the overall depths for events far offshore to the north, west

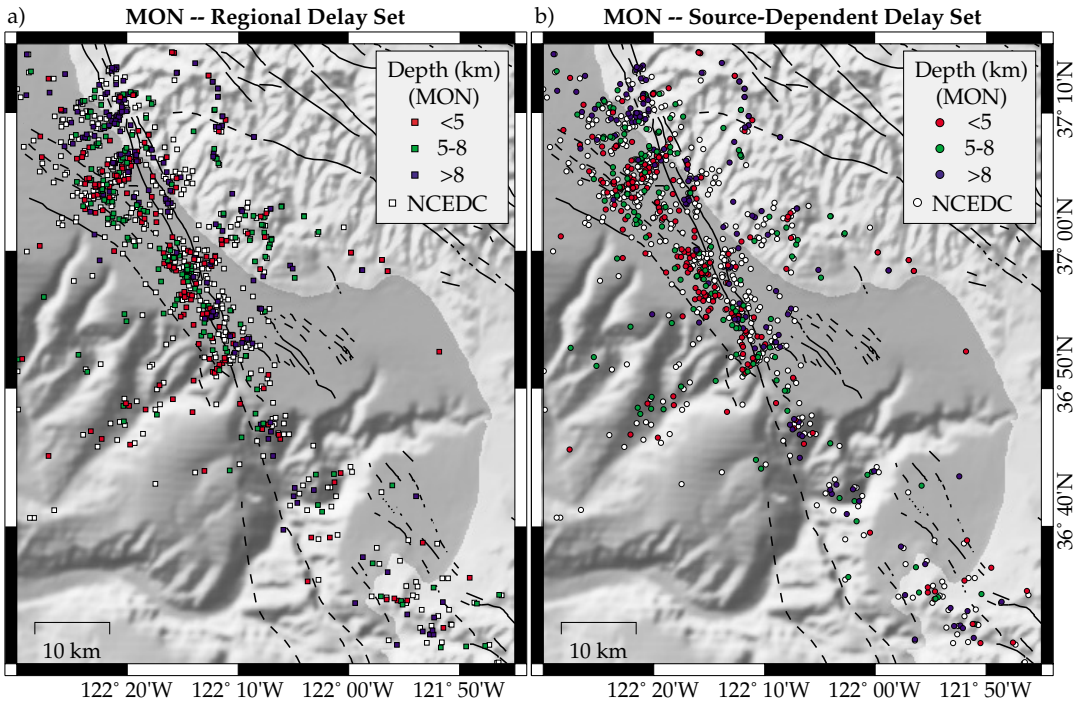

Figure 10. Relocations of the 1984–March 1999 data set using the MON model with (a) station delays determined for the entire region and (b) station delays specific to the northern, central, southern, and western areas of Monterey Bay. Both sets of relocations display less scatter in location and depth than the NCEDC locations (white symbols) and tend to locate more along mapped fault traces. Northern events, especially those west of the San Gregorio, tend to cluster in regions consistent with recent (1997–1999) seismicity patterns.

of the SGF (Fig. 10a and 11a). This is consistent with MON having slower velocities at shallow depths. Events located with the faster inland USGS models apparently cause locations to move farther and deeper offshore. The events west of the SGF trace also have relocated depths that are more compatible with fault depths determined using offshore seismic reflection data (S. Lewis and D. Caress, personal comm., 1999).

The locations using the source-dependent delay set display a further reduction in scatter compared to locations using the MON model with a single regional station delay set (Fig. 10). Events display clustering patterns near the SGF in northern MB, consistent with recent seismicity patterns (NCEDC; Begnaud and Stakes, 2000) showing "hot spots" of activity. In Figures 10–11, the epicenter positions suggest that shallow events ($< \sim 8$ km depth) are located on the western edge of the SGF or along the faults west of the SGF. Deeper (>8 km depth) events tend to have their epicenters along the eastern edge of the SGF, which is consistent with an east-dipping SGF, as found by McNally and Stakes (1998). They also found that focal mechanisms indicate that west of Santa Cruz, the SGF strikes at N27°W $\pm$ 3° and dips to the east at 61° $\pm$ 5° with primarily thrust motion and a component of right-oblique slip. The discovery of this dipping focal plane and thrust mechanisms is a potential hazard for the adjacent populated coastal region.

Events on the Monterey peninsula, to the south, also display less scattering when using the source-dependent delays and suggest a linear trend of activity oriented subparallel to the trend of Carmel Canyon with both shallow and deeper events (Figs. 10–11). Events west of the SGF in northern MB display linear trends perpendicular to the orientation of the SGF and nearby fault traces, but subparallel to the orientation of offshore submarine canyons. We cannot conclude here whether these patterns are real or artifacts of the location process, given the large azimuthal gap for these events, even when including offshore phase data. Further, there is a linear trend of relatively shallow (<8 km) events along the northern edge of Smooth Ridge, the fan-like structure just west of the central SGF (Fig. 2, 10–11). The structures in and around Smooth Ridge are not obvious, but this linear trend could indicate possible landslide activity within the canyon (with associated errors in hypocenter determination) or actual earthquakes related to a zone of weakening from compression and uplift of Smooth Ridge (Orange *et al.,* 1999).

The use of the MON model allows for more consistent locations and depths for SGF and MBFZ events, which then result in more consistent focal mechanism calculations. This

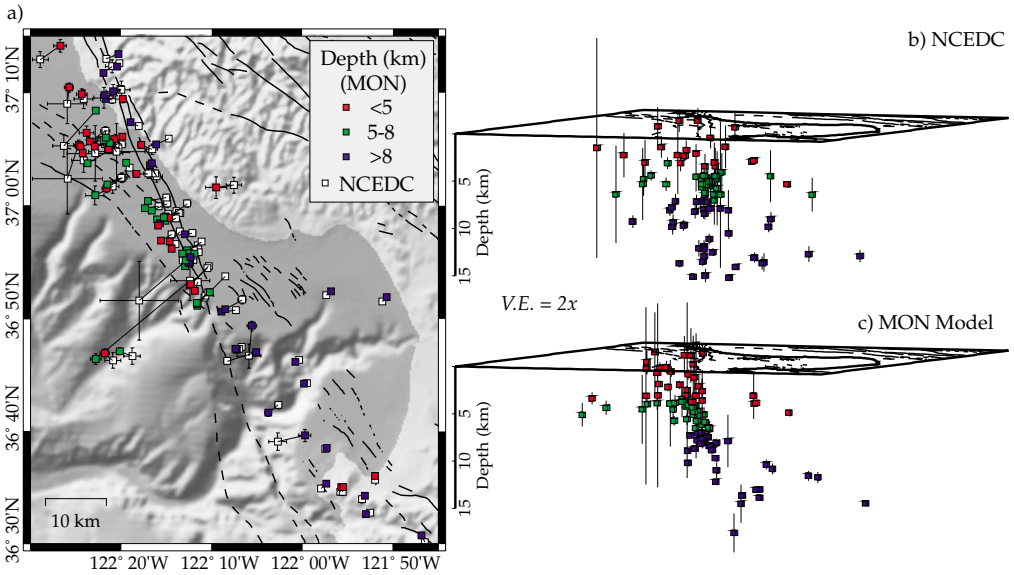

Figure 11. Relocations of the master events along with Monterey Bay events detected by the ocean-bottom and/or coastal Ref Tek instruments from June 1997–March 1999 (see Figure 2). Before relocation, the NCSN phases were reweighted as described in the section Phase Data in text. The MON model was used along with source-dependent station delays. (a) Epicenter changes after relocation using MON model. Events tend to cluster more along fault traces. (b) Three-dimensional view along trace of San Gregorio fault (azimuth 158°) for original NCEDC catalog locations using USGS velocity models. (c) Three-dimensional view of relocated events using MON model. Event scatter is reduced compared to catalog locations in (b). Events west of the San Gregorio tend to be shallow (<8 km), and the hypocenter pattern suggests an eastward dip for the San Gregorio fault.

has implications for fault hazard assessments for the MB area (McNally and Stakes, 1998; K. McNally *et al.,* unpublished data, 1999).

The differences in calculated station delays with respect to source region strongly suggest that MB has a high degree of lateral heterogeneity, at least in the upper crust. The MON model should be relatively faster for the northern and western SGF and slower for the southern SGF/MBFZ. This also suggests why there is a negative skew for the single regional delay set from Figure 9. The majority of events in the 1984–March 1999 data set are from the northern-central SGF area, which would bias the calculation of a single regional delay set.

Velocity Structure

Since there is no evidence for elevated temperatures within the upper crust of MB—the youngest volcanic rocks in the region have been dated at over 2 m.y. old (Dickinson, 1997)—the slower velocities in the upper 6 km calculated for the MON model are either the result of compositional differences, compared to the defined regions for USGS velocity models (Fig. 4), or, more likely, the result of intense fracturing of the upper crust from the MBFZ and its interaction with the SGF. From a three-dimensional (3D) velocity inversion for the San Francisco Bay area, Parsons and Zoback (1997) and Hole *et al.* (2000) found somewhat slower velocities (~4.7–5.3 km/sec) at a depth of ~4 km west of the SGF, directly north of MB. This is consistent with the slower velocities that we observe above ~6 km in the MON model, although they are faster by as much 0.8 km/sec. Another 3D velocity model by Eberhart-Phillips and Michael (1998) for the Loma Prieta area (east of MB) displays velocities of ~5.5 km/sec at a depth of 4 km, faster than the MON model. We note that both of the 3D velocity models above have the SGF/MBFZ region of MB located near the edges of the resolved model sections. A reflection/refraction profile perpendicular to the northern coast of MB (Brocher *et al.,* 1992; Page and Brocher, 1993) resulted in a model with velocities similar to those at 4 km depth for the 3D models above. The Ross model (Fig. 8) also does not display the slower velocities in the upper crust calculated for the MON model. None of these studies utilize offshore nor a large number of near-coastal instruments which suggests that the offshore/coastal component of this study is key in constraining the shallow slower velocities specific to the SGF and MBFZ.

MBARI ROV dives conducted since 1992 throughout the Monterey Canyon have provided a detailed geological map of the primary lithologies (Stakes *et al.,* 1999b). The 1200–1400 m deep canyon provides continuous exposures of basement rocks from north of Monterey Peninsula to Carmel Canyon. Visual descriptions supplemented by controlled sampling permits important geological checks on the

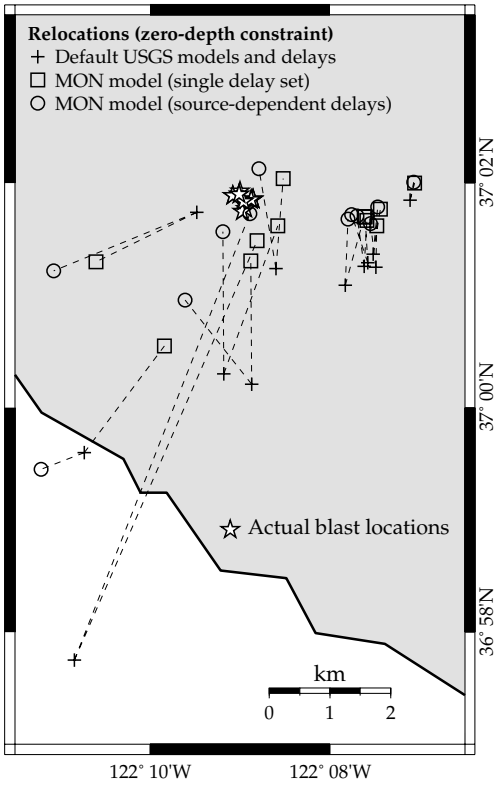

Figure 12. Relocations of blasts for a quarry in Davenport, California, ~10 miles northwest of Santa Cruz. All locations shown were calculated with a fixed depth at the surface. Tie lines indicate changes from using USGS velocity models (mainly the LOM model) (crosses) to using the MON model with a regional delay set (squares) and a delay set specific for the northern San Gregorio region (circles). Stars indicate actual blast locations within the quarry. The MON model produces more accurate locations, with the use of source-dependent delays being slightly more accurate for several blasts.

velocity model proposed here. The basement rocks on the east side of Monterey Canyon are coparallel with one of the strands of the MBFZ. Recovered drillcores of fault gouge derived solely from granitic material, ubiquitous slickensides, and carbonate veins suggest pervasive deformation and groundwater flow through open fractures. Basement exposures just north of the Monterey Peninsula have a high degree of fracturing. Narrow promontories (2–5 m wide) are separated by vertical sheer walls formed by recent landslides. The intense fracturing precluded the deployment of a borehole anywhere in this region because no intact bedrock could be found. To the north, the granodiorite basement dips steeply beneath the thick and well-bedded Miocene-Pliocene sediments, which comprise the only exposures on the west side of the Canyon. Cold seeps and their associated chemosynthetic communities are aligned along the still-active traces of the MBFZ where it crosscuts these sediments, apparently providing permeable conduits for fluid flow (Stakes *et al.,* 1999a). Fault traces exposed on the Monterey Peninsula are approximately coparallel to the MBFZ and juxtapose granodiorite of differing mineralogy and isotopic characteristics (Kistler and Champion, 1997), supporting the model of pervasive internal deformation, shearing and lateral offset within the Salinian block. Such brittle deformation would have the most impact on crustal velocities at shallow depths.

The faster velocities observed from ~16 to 25 km are not observed in any of the USGS 1D velocity models derived for the MB area (LOM, CST, PEN). This is not surprising given that we used many distant (>100 km) stations west of the San Andreas fault for the second step of the inversion process, causing more deep coast-parallel rays to be used in the velocity inversion. From Figure 5, it is clear that all starting models used in the inversion result in the faster velocities for the ~15–25 km depth zone and that the data require this structure. The transition zone in the MON model from 25 to 30 km may not be as well resolved; this indicates that the Moho could be shallower (~25–27 km) than the 30 km suggested by the MON model (Fig. 8).

Although none of the 1D USGS velocity models used for the area indicate any type of intermediate depth (15–30 km) structure, the 3D velocity inversions mentioned previously, two-dimensional seismic reflection/refraction surveys along the central California margin, and the 1D Monterey model do display this feature. The 3D inversions by Eberhart-Phillips and Michael (1998) and Hole *et al.* (2000) display velocities of ~6.5–6.9 km/sec at depths of ~18 km near the MB coast. The seismic reflection/refraction profiles for the central California coast shown in Tréhu (1991), Page and Brocher (1993), and Holbrook *et al.* (1996) are modeled with faster velocities (~6.4–7.3 km/sec) at greater than ~15 km depth. The Ross 1D model also displays faster velocities (~7 km/sec) at ~20 km depth.

The faster velocity zone beginning at greater than ~15 km suggests an intermediate composition between the overlying granitic crustal rock and the upper mantle at ~30 km. Many studies have suggested that the California continental margin is underlain by oceanic crust (Page and Brocher, 1993, and references therein). Nicholson *et al.* (1994) suggests that the Monterey Plate was accreted to the base of the crust during the late Oligocene-early Miocene. Thus the layer of intermediate composition at the base of the crust may be the remnant of the subducted Monterey Plate. The depth and apparent thickness of the faster-velocity layer in the MON model as well as other velocity models tend to support this view.

Conclusions

Our best 1D velocity model to ~30 km depth, and specific to the Monterey Bay coastal region, exhibits two new features not previously identified in other models used for earthquake location in this area. Above ~6 km, our new model is relatively slow (range: ~3–5.8 km/sec) which we

attribute to sheared granites, which have been observed on the seafloor, associated with intense faulting and/or fracturing along the SGF/MBFZ, especially where they intersect. These slower velocities are not observed for 1D velocity models surrounding MB, suggesting a local effect. The use of phases from MBARI ocean-bottom and coastal RefTek instruments were critical in constraining the shallow, slower velocities. Calculated source-dependent stations delays for the north, south, central, and west SGF/MBFZ events suggest lateral shallow heterogeneity for the region with faster velocities along the northern and western SGF area in MB and slower velocities along the central and southern SGF/MBFZ areas.

From ~16 to 25 km depth, our model is relatively fast (range: ~6.3–7.1 km/sec). This feature of the MON model is also not observed for surrounding 1D USGS velocity models and is probably the result of the inclusion of distant (>100 km) stations along the coast, west of the San Andreas fault into the velocity inversion. Other independently derived velocity models do display these faster velocities at depth, which we attribute to mafic materials emplaced through tectonic processes such as the presence of accreted oceanic crust.

In addition to structural features, earthquake relocations using the MON model, with either the single regional or source-dependent delay sets, results in improvements to the mean rms travel-time residual (17% and 25%, respectively) for the 1984–March 1999 earthquake data set. Relocations are more consistent with mapped fault traces, patterns of recent seismicity, and an east-dipping SGF.

This velocity model can serve as a reliable starting model for two and three-dimensional modeling of MB area velocity structure. It will also be useful for more reliable and consistent earthquake locations and focal mechanism determinations for the area.

Acknowledgments

The authors wish to thank the pilots of the ROV Ventana and the crew of the R/V Pt. Lobos for their excellent work with the ocean-bottom deployments. We also wish to thank Gerry Simila, Karen Salamy, Paul McGill, Jesse Williams, George Badger, and Russell Sell for their assistance with instrument deployments and data processing. Special thanks to IRIS for the use of their RefTeks and to Jim Lake and the staff of the RMC Lone Star Cement Company for their contribution of the blast locations. We acknowledge the contribution of the NCEDC and the USGS public data sets. The comments from Marcia McNutt, David Caress, Stephanie Ross, and an anonymous reviewer greatly improved the quality of this article. Support for this project was provided by the Lucile and David Packard Foundation. Partial support was provided by the Lawrence Livermore National Laboratory and University of California, Santa Cruz.

References

Begnaud, M. L., and D. S. Stakes (2000). Constraining continental margin seismicity by extending on-shore seismograph stations to critical offshore sites, *Bull. Seism. Soc. Am.* **90,** 414–424.

Brocher, T. M., M. J. Moses, and S. D. Lewis (1992). Wide-angle seismic recordings obtained during seismic reflection profiling by the S. P. Lee offshore the Loma Prieta epicenter, *U.S. Geol. Surv. Open-File Rept. 92-245,* 63 pp.

Clark, J. C., E. E. Brabb, H. G. Greene, and D. C. Ross (1984). Geology of the Pt. Reyes Peninsula and implications for the San Gregorio fault history, in *Tectonics and Sedimentation along the California Margin, Spec. Publ. 38,* J. K. Crouch and S. B. Backman (Editors), Guidebook Pacific Section, Society of Economic Paleontologists and Mineralogists, Los Angeles, California, 67–86.

Clark, J. C., G. E. Weber, L. I. Roserberg, and K. Burnham (1999). Neotectonics of the San Gregorio Fault Zone, Central Coast California, Field Trip Guide 2, in *Late Cenozoic fluid seeps and tectonics along the San Gregorio fault zone in the Monterey Bay region, California,* R. E. Garrison, I. W. Aiello, and J. C. Moore (Editors), Guidebook Pacific Section, American Association of Petroleum Geologists GB-76, Camarillo, California, 121–156.

Dickinson, W. R. (1997). Tectonic implications of Cenozoic volcanism in coastal California, *Geol. Soc. Am. Bull.* **109,** 936–954.

Dietz, L. D., and W. L. Ellsworth (1990). The October 17, 1989, Loma Prieta, California, earthquake and its aftershocks: geometry of the sequence from high-resolution locations, *Geophys. Res. Lett.* **17,** 1417–1420.

Dorbath, C., D. Oppenheimer, F. Amelung, and G. King (1996). Seismic tomography and deformation modeling of the junction of the San Andreas and Calaveras faults, *J. Geophys. Res.* **101,** 27,917–27,941.

Eberhart-Phillips, D., and A. J. Michael (1998). Seismotectonics of the Loma Prieta, California, region determined from three-dimensional Vp, Vp/Vs, and seismicity, *J. Geophys. Res.* **103,** 21,099–21,120.

Graham, S. A., and W. R. Dickinson (1978). Apparent offsets of on-land geologic features across the San Gregorio-Hosgri fault trend, in *San Gregorio-Hosgri Fault Zone, California,* E. A. Silver and W. R. Normark (Editors), Calif. Div. Mines Geol. *Spec. Rept. 137,* 13–23.

Greene, H. G. (1990). Regional tectonics and structural evolution on the Monterey Bay region, central California, in *Geology and Tectonics of the Central California Coastal Region, San Francisco to Monterey,* R. E. Garrison, H. G. Greene, K. R. Hicks, G. E. Weber and T. L. Wright (Editors), Guidebook Pacific Section, American Association of Petroleum Geologists 67, Camarillo, California, 31–56.

Holbrook, W. S., T. M. Brocher, U. S. ten Brink, and J. A. Hole (1996). Crustal structure of a transform plate boundary: San Francisco Bay and the Central California continental margin, *J. Geophys. Res.* **101,** 22,311–22,334.

Hole, J. A., T. M. Brocher, S. L. Klemperer, T. Parsons, H. M. Benz, and K. P. Furlong (2000). Three-dimensional seismic velocity structure of the San Francisco Bay area, *J. Geophys. Res.* **105,** 13,859–13,874.

Kelson, K. I., W. R. Lettis, and M. Lisowski (1992). Distribution of geologic slip and creep along faults in the San Francisco Bay region, in *Proc. of the Second Conference on Earthquake Hazards in the Eastern San Francisco Bay Area, California Department of Conservation, Div. Mines Geol. Spec. Publ. 113,* 31–38.

Kissling, E., W. L. Ellsworth, D. Eberhart-Phillips, and U. Kradolfer (1994). Initial reference models in local earthquake tomography, *J. Geophys. Res.* **99,** 19,635–19,646.

Kistler, R. W., and D. E. Champion (1997). Ages of hornblende and biotite from plutons in the Salinian block, coastal California, *Geol. Soc. Am. Abstr.* **29,** 22.

Klein, F. W. (1989). User's guide to HYPOINVERSE, a program for VAX computers to solve for earthquake locations and magnitudes, *U.S. Geol. Surv. Open-File Rept. 89-314,* 44 pp.

McNally, K. C., and D. S. Stakes (1998). Implications of the San Gregorio fault zone seismicity for Monterey Bay coastal hazard assessment (abstract), *EOS Trans. AGU* **79,** F589.

Nicholson, C., C. C. Sorlien, T. Atwater, J. C. Crowell, and B. P. Luyendyk (1994). Microplate capture, rotation of the western Transverse Ranges, and initiation of the San Andreas transform as a low-angle fault system, *Geology* **22,** 491–495.

Olson, J. A. (1986). Seismicity of the San Andreas fault zone in the San

Francisco peninsula area, California, *R. Soc. New Zealand Bull.* **24,** 87–97.

Oppenheimer, D., F. W. Klein, J. P. Eaton, and F. Lester (1993). The Northern California Seismic Network Bulletin January–December 1992, *U.S. Geol. Surv. Open-File Rept. 93-578,* 45 pp. (Available at http://quake.geo.berkeley.edu/ncsn/bulletin.ps)

Orange, D. L., H. G. Greene, D. Reed, J. B. Martin, C. M. McHugh, W. B. F. Ryan, N. Maher, D. Stakes, and J. Barry (1999). Widespread fluid expulsion on a translational continental margin: mud volcanoes, fault zones, headless canyons, and organic-rich substrate in Monterey Bay, California, *Geol. Soc. Am. Bull.* **111,** 992–1009.

Page, B. M., and T. M. Brocher (1993). Thrusting of the central California margin over the edge of the Pacific plate during the transform regime, *Geology* **21,** 635–638.

Parsons, T., and M. L. Zoback (1997). Three-dimensional upper crustal velocity structure beneath San Francisco peninsula, California, *J. Geophys. Res.* **102,** 5473–5490.

Peterson, M., T. Toppozada, T. Cao, C. Cramer, M. Reichle, M. Maher, and L. Atchison (1998). New geologic maps lend support to better building design in California earthquake country, *Calif. Geol.* **51,** 3–9.

Romanowicz, B., D. Neuhauser, B. Bogaert, and D. Oppenheimer (1994). Accessing northern California earthquake data via internet, *EOS Trans. AGU* **75,** 258–261.

Romanowicz, B., D. Stakes, J. P. Montagner, P. Tarits, R. Uhrhammer, M. Begnaud, E. Stutzman, M. Pasyanos, J. F. Karczewski, S. Etchemendy, and D. Neuhauser (1998). MOISE: a pilot experiment towards long term sea-floor geophysical observatories, *Earth Planets Space* **50,** 920–937.

Simpson, G. D., S. C. Thompson, J. S. Noller, and W. R. Lettis (1997). The northern San Gregorio fault zone: evidence for the timing of late Holocene earthquakes near Seal Cove, California, *Bull. Seism. Soc. Am.* **87,** 1158–1170.

Stakes, D., J. McClain, T. VanZandt, P. McGill, and M. Begnaud (1998a). Corehole seismometer development for low-noise seismic data in a long-term seafloor observatory, *Geophys. Res. Lett.* **25,** 2745–2748.

Stakes, D. S., B. Romanowicz, J. P. Montagner, P. Tarits, J. F. Karczewski, S. Etchemendy, C. Dawe, D. Neuhauser, P. McGill, J. C. Koenig, J. Savary, M. Begnaud, and M. Pasyanos (1998b). Seismic experiment paves way for long-term seafloor observatories, *EOS Trans. AGU* **79,** no. 301, 308–309.

Stakes, D. S., D. Orange, J. B. Paduan, K. A. Salamy, and N. Maher (1999a). Cold-seeps and authigenic carbonate formation in Monterey Bay, California, *Mar. Geol.* **159,** 92–109.

Stakes, D. S., C. A. Rigsby, and P. C. Baucom (1999b). Igneous and sedimentary rocks from Monterey Canyon, California and implications for regional tectonics, in *Late Cenozoic Fluid Seeps and Tectonics along the San Gregorio Fault Zone in the Monterey Bay Region, California,* R. E. Garrison, I. W. Aiello, and J. C. Moore (Editors), Pacific Section, American Association of Petroleum Geologists GB-76, Camarillo, California, 75–92.

Tréhu, A. (1991). Tracing the subducted oceanic crust beneath the central California continental margin: results from ocean bottom seismometers deployed during the 1986 Pacific Gas and Electric EDGE experiment, *J. Geophys. Res.* **96,** 6493–6506.

Weber, G. E. (1990). Late Pleistocene slip rates on the San Gregorio fault zone at Point Año Nuevo, San Mateo County, California, in *Geology and Tectonics of the Central California Coastal Region, San Francisco to Monterey,* R. E. Garrison, H. G. Greene, K. R. Hicks, G. E. Weber and T. L. Wright (Editors), Guidebook Pacific Section, American Association of Petroleum Geologists 67, Camarillo, California, 193–203.

Working Group on Northern California Earthquake Potential (1996). Database of potential sources for earthquakes larger than magnitude 6 in northern California, *U.S. Geol. Surv. Open-File Rept. 96-705,* 57 pp. (Available at http://quake.wr.usgs.gov/hazprep/NCEP)

Monterey Bay Aquarium Research Institute
7700 Sandholdt Road
Moss Landing, California, 95039
(M.L.B., D.S.S., V.A.G.)

Earth Science Department and Institute of Tectonics
University of California
1156 High Street
Santa Cruz, California, 95064
(K.C.M., V.A.G.)

Manuscript received 31 January 2000.